

Reduced Circular Field-of-View Imaging

Klaus Scheffler, Jürgen Hennig

A rapid dynamic imaging technique based on polar k -space sampling is presented. A gain in temporal resolution is achieved by angular undersampling. A detailed analysis of the point spread function of angular undersampled polar imaging reveals a reduced diameter of the corresponding circular field of view. Under the assumption that dynamic changes are restricted to a local circular field of view, angular undersampled dynamic imaging allows the recording of rapid changes at high temporal and spatial resolution. The theoretical and experimental details of the technique are presented. Key words: polar imaging; dynamic imaging; angular undersampling; interventional MRI.

INTRODUCTION

With the recent advances in gradient hardware and sequences design, rapid dynamic imaging has become a widely used technique. There are essentially two ways to increase imaging speed: a faster scanning of k -space or a reduction of k -space coverage. Rapid k -space traverse such as echo-planar trajectories (1) requires dedicated gradient amplifiers, and their performance is restricted by physiological stimulation limits (2). The half Fourier technique is the most popular example for reduced k -space sampling (3). It has equal resolution in comparison with full k -space coverage but exhibits a signal-to-noise ratio reduced by $\sqrt{2}$. The keyhole technique or k -space substitution is based on a reduction of image resolution in phase encode direction by confining the phase encodes to the k -space center (4, 5). As a result, it is less suitable for applications where high spatial resolution of the dynamic information is required. Locally focused imaging described by Yao *et al.* (6) is a novel technique that permits the specification of arbitrary spatial resolution in arbitrary 2D regions. The images are reconstructed from sparsely sampled and cleverly, non-uniformly distributed k -space data, thus reducing acquisition time.

A further possibility that is comparable to the method proposed in this paper is reduced field-of-view (FOV) imaging, introduced by Hu and Parrish (7). This method is based on the assumption that the changes in a dynamic study are sometimes localized to a small rectangular area within the entire FOV. These changes can be recorded by a reduced but uniform sampling density of the k -space in

phase encode direction and, thus, with an increased imaging speed.

In this paper, we describe a novel reduced FOV technique based on radial sampling. The angular sampling density is reduced to improve temporal resolution. Angular undersampling reduces the radius of the corresponding circular FOV and, therefore, allows dynamic studies of localized changes. The relationship between angular and radial sampling density and the resulting point spread function of the imaging process is discussed in detail in the THEORY section. We also investigate novel sampling patterns, such as nonconstant angular density functions, and the possibility of generating non-circular FOVs. Reconstruction algorithms and implementation of the reduced circular FOV technique are described in the Implementation section. Experimental results, robustness, and possible artifacts of the new technique will be analyzed.

THEORY

Properties of the Polar Point Spread Function

MR images are reconstructed from a limited number of k -space samples. The resulting image degradation is usually described by the point spread function (PSF) of the corresponding imaging process. Most imaging sequences sample k -space on a rectangular grid, resulting in the well-known Dirichlet-shaped PSF (8). For polar sampling, k -space data are acquired on equidistant spacings in radial k_r and angular k_θ direction. As usual, the relation between polar and Cartesian coordinate systems is given by $k_x = k_r \cos k_\theta$, $k_y = k_r \sin k_\theta$ in k -space and $x = r \cos \theta$, $y = r \sin \theta$ in object space. The polar sampling function $S(k_r, k_\theta)$, then, is a sum over the product of two delta functions

$$S(k_r, k_\theta) = \Delta k_\theta \Delta k_r \sum_{n_\theta=0}^{N_\theta-1} \sum_{n_r=0}^{N_r-1} \delta(k_\theta - n_\theta \Delta k_\theta) \delta(k_r - n_r \Delta k_r) \quad [1]$$

N_θ is the number of projections separated by the angular increment of $\Delta k_\theta = 2\pi/N_\theta$, and N_r is the number of samples in k_r direction with radial increment Δk_r . The resulting PSF is given by the Fourier transformation in polar coordinates of the sampling function S

$$\text{PSF}(r, \theta) = \int_{k_\theta=0}^{\pi} \int_{k_r=0}^{\infty} S(k_r, k_\theta) e^{2\pi i r k_r \cos(k_\theta - \theta)} |k_r| dk_\theta dk_r \quad [2]$$

$$S(k_r, k_\theta) e^{2\pi i r k_r \cos(k_\theta - \theta)} |k_r| dk_\theta dk_r$$

This integral can be simplified for several types of sampling patterns. We will investigate five special cases of polar sampling patterns in detail, namely, continuous

MRM 40:474-480 (1998)

From the MR-Center of the University (K.S.), Basel, Switzerland; and Radiologische Klinik (J.H.), Röntgendiagnostik, MR-Tomographie, Freiburg, Germany.

Address correspondence to: Klaus Scheffler, Ph.D., MR-Center of the University Basel, Klingelbergstrasse 50, 4031 Basel, Switzerland.

Received September 27, 1997; revised January 15, 1998; accepted March 4, 1998.

This work was supported by the Swiss National Foundation under Grant 31.32533.91.

0740-3194/98 \$3.00

Copyright © 1998 by Williams & Wilkins

All rights of reproduction in any form reserved.

sampling in angular and radial direction, discrete angular undersampling, optimal sampling, and angular oversampling.

Continuous Sampling

Continuous sampling in angular direction as depicted in Fig. 1a was investigated by Lauzon and Rutt (9), based on the work of Bracewell and Thompson (10). For this ring-like sampling, Eq. [2] reduces to

$$\text{PSF}(r) = 2\pi(\Delta k_r)^2 \sum_{n_r=1}^{N_r-1} n_r J_0(2\pi\Delta k_r n_r r) \quad [3]$$

which is a sum over zero-order Bessel functions J_0 . The 2D PSF and an intensity profile along the radial dimension are plotted in Fig. 1a. The concentric ring lobes surrounding the main peak at $r = 0$ are responsible for the radial aliasing artifact (Fig. 1a, right) that occurs when the object size exceeds the circular FOV with the diameter of $1/\Delta k_r$.

Continuous radial sampling, as shown in Fig. 1b, leads to a completely different shape of the corresponding PSF. The coefficients of the Fourier-Bessel integral become independent of k_r , and the corresponding integrals $\int k_r J_n(2\pi k_r r) dr$ diverge. The extent of sampling in radial direction k_r in k -space must, therefore, be limited to a finite value of k_R ; otherwise, the total measuring time and the signal power become infinite. Computation of Eq. [2] results in

$$\text{PSF}(r, \theta) = 2\Delta k_\theta \sum_{n_\theta=0}^{N_\theta-1} \left(\frac{\cos(a_{n_\theta} k_R) + a_{n_\theta} k_R \sin(a_{n_\theta} k_R) - 1}{a_{n_\theta}^2} \right) \quad [4]$$

where a_{n_θ} is given by $a_{n_\theta} = 2\pi r \cos(n_\theta \Delta k_\theta - \theta)$. The PSF consists of radial stripes in the sampling direction (Fig. 1b) that produce streak artifacts. The intensity plot along the angular coordinate θ for a fixed distance r in Fig. 1b is similar to the Dirichlet kernel of Cartesian sampling.

Discrete Sampling

In real life, sampling is generally limited to a finite number of k -space data. The principle of reduced circular FOV imaging is based on angular, undersampled discrete polar sampling. The following three different types of polar grid sampling (Figs. 1c–1e) demonstrate the relation between angular sampling density, the resulting PSF, and image degradation.

For Cartesian sampling, the FOV is defined by the sampling distances Δk_x and Δk_y in k -space. A similar relationship can be found for discrete polar sampling. We define $\Delta k_\theta^{\max} = 2\pi\Delta k_r N_r / N_\theta$ to be the maximal distance between two neighboring samples in angular direction (Fig. 1c, left). For angular undersampling (Fig. 1c), the radial increment Δk_r is much smaller than the maximal angular increment Δk_θ^{\max} or, equally, the number of radial steps N_r is much larger than the number of angular steps N_θ . Discrete angular undersampling is similar to the previous case of continuous radial sampling and leads to

a starlike PSF. However, this PSF shows a small circular flat region at its center, which can also be identified in the corresponding radial intensity profile. Angular undersampling allows, therefore, artifact-free imaging as long as the extension of the object does not exceed the radius of this reduced circular FOV. Otherwise, typical streaking artifacts, as shown on the right in Fig. 1c and Fig. 2, will appear in the image.

An increase in the sampling density in angular direction leads to an intermediate state of optimal sampling (Fig. 1d). The circular flat region of the PSF linearly expands to the first ring lobe, which is responsible for the radial aliasing effect. Numerical computation of the PSF, given by Eq. [3], shows that the expansion of the flat circular region up to the first ring is given by the condition $\Delta k_r = \Delta k_\theta^{\max}$ or $N_\theta = 2\pi N_r$. The same result was derived by Natterer for parallel beam CT (11). The intensity profile in the radial direction in Fig. 1d is composed of two parts. Within the interval $[-r\Delta k_r, r\Delta k_r]$, the profile is approximately given by the Bessel functions of Eq. [3] and, therefore, is similar to continuous angular sampling. Beyond the first ring lobe, wild oscillations occur. Beside radial aliasing artifacts, an object that exceeds the FOV will, therefore, produce additional streaking artifacts.

Angular oversampling as depicted in Fig. 1e on the left is similar to the first type of continuous angular sampling. The PSF shows equidistant ring lobes surrounding the main center peak. The amplitude of successive rings decreases as a function of the radial distance k_r , which is proportional to k_r^{-2} . The Bessel-like intensity profile is now limited to a larger extent of $\pm 1.4r\Delta k_r$, according to the increased number of angular samples (70 for Fig. 1e, and 50 for Fig. 1d).

The previous numerical examples on polar PSF show a basic and important difference compared with Cartesian sampling. Polar sampling generally produces streaking and radial aliasing artifacts. These artifacts appear inside or outside the circular FOV depending on the size of the object. Even for optimal polar sampling (Fig. 1d), streaks and rings can be observed outside the displayed window (Fig. 1d, right). By contrast, the Dirichlet-shaped PSF of Cartesian sampling just generates an infinite amount of identical copies of the object, separated by the dimensions of the rectangular FOV.

Reduced Circular FOV Imaging Technique

Reduced circular FOV imaging is a rapid imaging technique that allows the measurement of dynamic changes within a small region of interest, which is located inside a large surrounding object. This zooming technique is based on angular undersampled polar imaging (12, 13). A decrease in angular sampling density N_θ causes a decrease in the radius R of the circular flat region of the PSF; see Figs. 1c–1e. For optimal sampling ($N_\theta = 2\pi N_r$, Fig. 1d), R is equal to $1/\Delta k_r$, and angular undersampling reduces R by the factor $N_\theta/2\pi N_r$.

$$R = \frac{1}{\Delta k_r} \frac{N_\theta}{2\pi N_r} \leq \frac{1}{\Delta k_r} \quad \text{for } N_\theta \leq 2\pi N_r \quad [5]$$

An example of fourfold angular undersampling is shown in Fig. 2. A single leg smaller than the reduced FOV

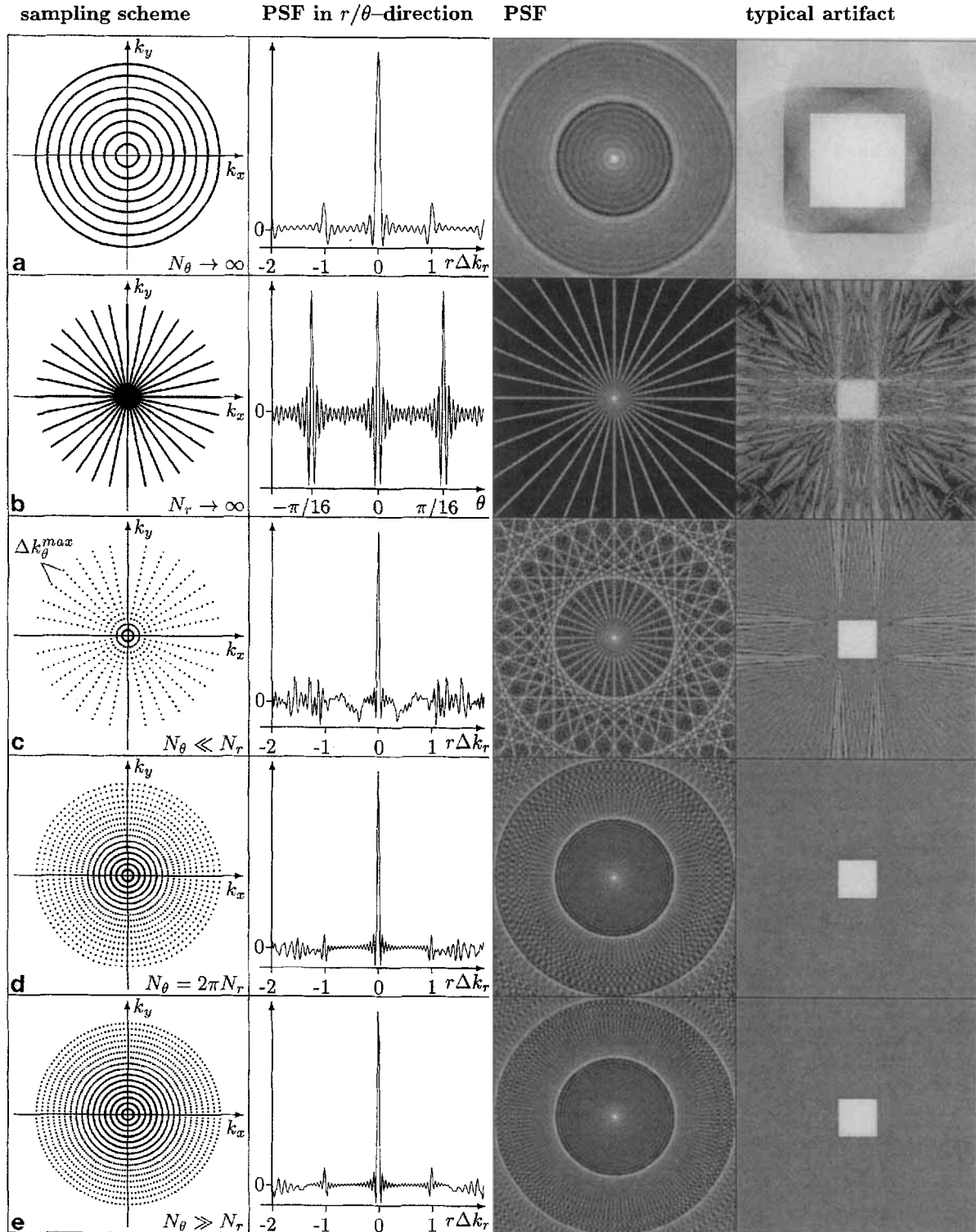


FIG. 1. Five different polar sampling patterns, the corresponding PSF, and typical imaging artifacts are shown in (a) to (e). The gray values of the half-tone magnitude images are printed with increased brightness and contrast. Continuous sampling in angular direction (a) generates a radially symmetric PSF composed of increasing principal rings. The resulting circular FOV has a diameter equal to the distance between the central peak and the first principal ring of the PSF. Radial aliasing artifacts appear if the object size exceeds the diameter of the FOV (right image in (a)). Continuous sampling in radial direction (b) generates a starlike PSF. An intensity profile in angular direction is shown in the second figure of (b). Intense streaking artifacts appear in the image of a square object. Discrete angular undersampling (c), optimal sampling (d), and angular oversampling (e) show different types of PSF that are a combination of the two continuous PSFs of (a) and (b). The diameter of the circular flat region at the center of the PSF is proportional to the ratio N_θ/N_r . This region is surrounded by equidistant principal rings and a number of tangential and radial stripes. Small objects can be imaged without streaking artifacts using a reduced circular FOV (c). The FOV can be adapted to the extension of the object, and imaging time can be saved.

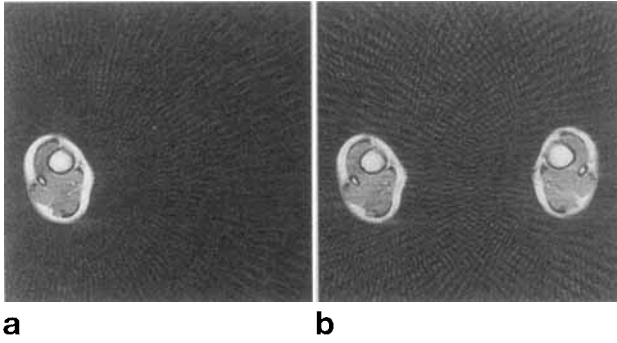


FIG. 2. T_1 -weighted polar imaging with reduced angular sampling density. Eighty-eight projections (within 360 degrees) and 128 samples (within zero and k_R) were used for both images, resulting in a fourfold reduced circular FOV of 75-mm diameter. (a) shows no artifacts within the FOV, whereas significant streaking artifacts are visible for both legs in (b).

produces no artifact (Fig. 2a). Typical streaking artifacts appear in Fig. 2b if a second leg exceeds the reduced FOV.

Reduced circular FOV imaging is based on the assumption that changes from image to image are located within a radially reduced FOV. These changes, therefore, can be recorded without artifacts by angular undersampled polar imaging. Reduction of imaging time is obviously proportional to the radius of the reduced circular FOV (in which the dynamic change occurs) or to the undersampling factor $N_\theta/2\pi N_r$. It is important to remark that reduction of measuring time is based on a reduction of the circular FOV without any loss in image resolution. The artifact-free reconstruction of the dynamic images from undersampled angular data based on the first reference scan is described in the IMPLEMENTATION section.

Noncircular Field of View

A noncircular FOV can be produced if Δk_θ varies as a function of the angular coordinate k_θ . An increased angular sampling density Δk_θ increases the radial extension of the corresponding FOV and vice versa. A π periodic angular density function, i.e., $\Delta k_\theta(n_\theta) = \Delta k_\theta(n_\theta + N_\theta/2)$, then, results in a point symmetric oval or elliptic FOV.

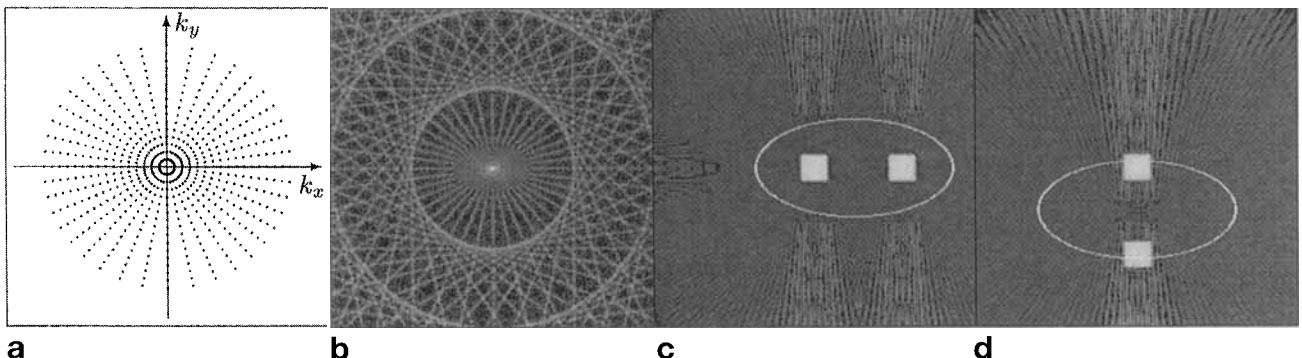


FIG. 3. Noncircular FOV polar imaging. A π periodic variation of the angular sampling density generates an elliptic or oval-shaped FOV. A reduction of angular density (in k_y direction (a)) results in a reduced diameter of the FOV (in y direction in (b)). Artifacts appear outside the reduced FOV (c) if the two squares are aligned in x direction. Both objects are disturbed by streaking artifacts in (d), where the distance of the two squares in y direction exceeds the nonisotropic FOV. Gray values are printed with increased brightness and contrast.

An example is shown in Fig. 3, where Δk_θ varies quadratically. The resulting anisotropic FOV, marked as white ovals, and its corresponding PSF produce artifact-free images if the objects are placed along the long axis (Fig. 3c) and streaking artifacts if both squares exceed the short axis of the FOV (Fig. 3d). A special case is lino-grams (14), where k -space diagonals start and end on a Cartesian grid. The angular sampling density is reduced along the principal axis, reflecting a reduced diameter of the FOV in x and y direction.

The use of a noncircular FOV for dynamic polar imaging is obvious. The restricted FOV in which dynamic processes occur is not limited to circular shapes, as for uniform angular undersampling, but can be matched, more or less, to anatomical requirements.

IMPLEMENTATION

A true FISP sequence (15) for polar imaging was implemented on a 1.5 T Siemens Vision scanner. In contrast with a spoiled (constant phase accumulation in a fixed direction between α pulses) FLASH type sequence, true FISP as depicted in Fig. 4 is favorable for fast back projection imaging, since zero phase accumulation requires minimal gradient switching time. This basically T_2 -weighted sequence was also used as a T_1 -weighted RF spoiled sequence by converting the initially constant RF phases to quadratically increasing phase steps (16) and by omitting the second rewinder of the slice gradient. The acquisition parameters were centered echo with $TE = 4.2$ ms, $TR = 9.0$ ms, receiver bandwidth of 83 kHz, a pulse angle of 70 degrees, and a circular FOV of 300-mm diameter (for optimal sampling). The acquisition time for an entire data set using 400 k -space diagonals (within $[0, \pi]$) and 256 samples (within $\pm k_R$) was 3600 ms. Eightfold and 16-fold angular undersampling, shown in the following examples, increased the time resolution to 450 and 225 ms, and reduced the dynamic FOV to approximately 38 and 19 mm, respectively.

Image Reconstruction from Projections

There are at least two basic methods for reconstructing MR images from polar sampled k -space data. Convolu-

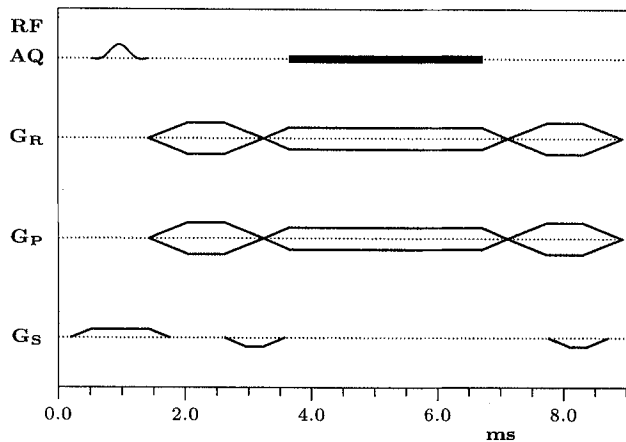


FIG. 4. Completely balanced gradient-echo sequence (true FISP) for polar sampling. The read and phase gradient (G_R and G_P) amplitudes are stepped according to a sine and cosine table. For T_1 weighting, RF spoiling was used and the second slice rewinder gradient was omitted.

tion back projection (11) is the classic technique developed for parallel and fan beam CT and is also implemented on some clinical MR systems. Another, more universal method is the mapping of k -space samples onto a Cartesian grid by interpolation techniques, followed by a complex Fourier transform. We prefer the gridding technique that, compared with convolution back projection, calculates complex images. Nonequidistant angular increments are easy to handle, and the computational effort is less. A cosine windowed sinc kernel (8), given by $\cos(\pi x / (2 \times \text{width})) \sin(\pi x) / \pi x$, was used for interpolation. The width of the kernel was set to three Cartesian increments (width = 3). Polar samples were weighted according to their density in k -space, which is inversely proportional to the radial distance k_r .

In practice, gridding of polar samples requires a carefully adjusted scanner or additional correction procedures. The main source of image artifacts is the delay times of the gradient amplifiers that influence the position of the echo maximum within the acquisition interval. A well-known example is the mismatch of even and odd echos in conventional EPI. For polar sampling, the echo position becomes a function of the angle k_θ and, therefore, has to be adjusted for each k -space diagonal by linear and constant phase correction.

Reduced Circular FOV Technique

The following steps to calculate dynamic images are visualized in Fig. 5. A first optimally sampled full FOV image is used as a reference image, Fig. 5a. Dynamic images are then acquired by eight- or 16-fold angular undersampling. An example is presented in Fig. 5b, showing the typical streaking artifacts. In the next step, difference images are calculated by subtraction of corresponding k -space diagonals of the reference image from the dynamic image. The result is an eight- or 16-fold angularly undersampled difference image, as shown in Fig. 5c. The difference image shows no artifacts as long as image differences are located within the reduced circular FOV (white ring in Fig. 5c). In a last step, the reduced

circular difference image is added to the full FOV image to complete the dynamic image with the static parts of the reference image, Fig. 5d. All operations are on complex values.

A critical point in terms of scanner stability, signal-to-noise ratio (SNR), and motion-related signal phase changes is the subtraction procedure to calculate the dynamic difference images. Separate imaging sequences for the reference scan and the dynamic scan additionally revealed slight artifacts in the difference images, probably induced by different eddy currents. We, therefore, implemented an interleaved acquisition scheme consisting of eight or 16 successive eight- or 16-fold angular undersampled k -space scans, each rotated by one angular increment. A comparable technique was used by Hu and Parrish for Cartesian interleaved sampling (7). A further advantage of interleaving is the possibility of completely updating the image information after eight or 16 dynamic scans, which can be used as a new reference image.

RESULTS

Dynamic polar imaging was validated on a grapefruit phantom. A time resolution of 225 ms was achieved by 16-fold undersampling. The corresponding reduced FOV, therefore, had a diameter of 19 mm. The cropped image series (Fig. 6) shows a dilation catheter that was placed in the center of a grapefruit. The reference image, reconstructed from 400 diagonal k -space scans, is shown in the upper left corner of Fig. 6. Water was pressed into

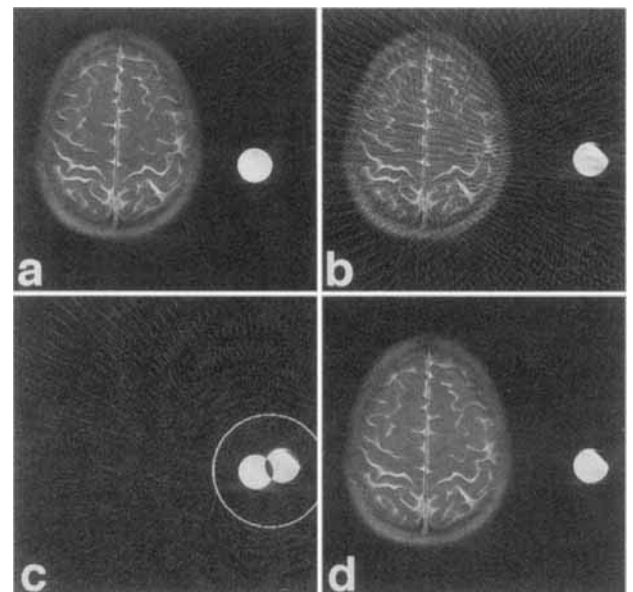


FIG. 5. Scan and calculation technique for dynamic polar imaging. (a) shows the static reference image acquired with 400 projections. In (b), the small water sphere was moved right about 15 mm, and an eightfold angular undersampled image (50 projections) was acquired. Typical streaking artifacts are visible. (c) is the difference image of (a) and (b) calculated by subtraction of corresponding k -space diagonals. No artifacts are visible within the reduced FOV (white ring). The (complex) sum of the reduced FOV in (c) and the reference image (a) finally generates the dynamic image (d).

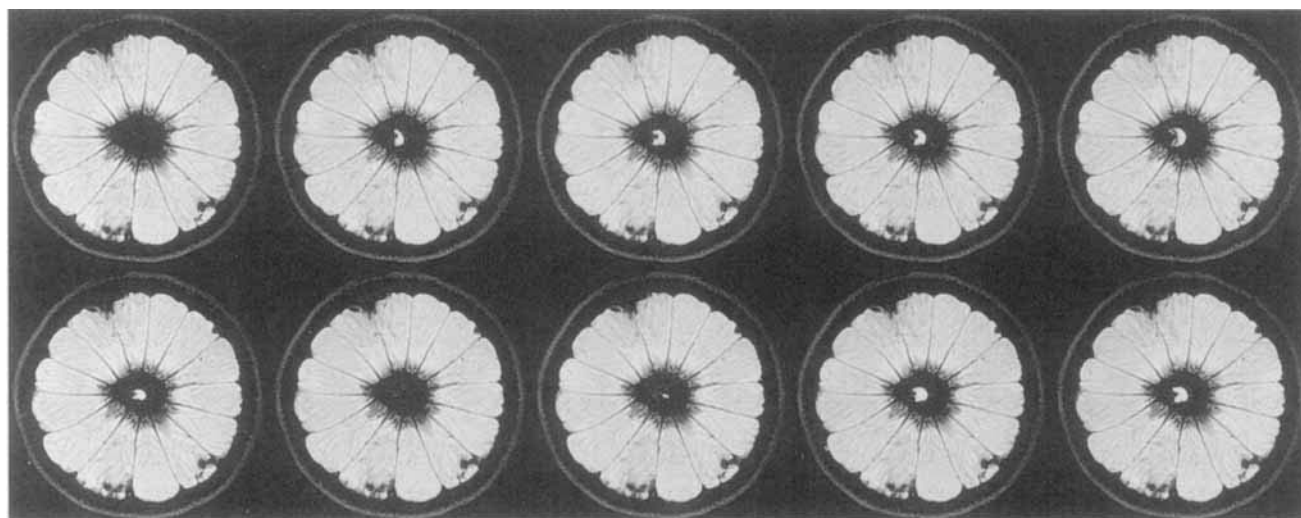


FIG. 6. Dynamic imaging of filling and emptying of a dilation catheter placed inside a grapefruit. The reference image, reconstructed from 400 diagonal k -space scans, is shown in the upper left corner. The dynamic series starts at the second image, running from left to right. Sixteenfold angular undersampling was used, corresponding to a reduced FOV of 19-mm diameter and a time resolution of 225 ms.

the catheter, and the continuous filling and emptying of the balloon was visualized in the dynamic imaging slices (second to last image). These images show a reduced SNR and a slight blurring artifact within the reduced FOV compared with the reference image. These artifacts are typical for polar imaging and are due to motion of the tube within the reduced acquisition time of 225 ms.

Dynamic polar imaging assumes that changes are located within a small region. Extensive changes lead to artifacts in the difference images, as shown in Fig. 7. The reference image was a head without water tube. Two eightfold angular undersampled images were then acquired in the presence of the water tube. The head was rotated by a few degrees for the second dynamic image. The difference image in Fig. 7a (fixed head) shows almost no artifacts. A susceptibility change or a difference in coil loading induced by the water tube could be responsible for the residual intensity of the head. Figure 7b shows the water tube and the difference in the two head

positions. Here, the difference image exceeds the reduced FOV of 38 mm, and weak streaking artifacts become visible.

DISCUSSION AND CONCLUSION

The phantom studies show that reduced circular FOV imaging is able to generate dynamic images with high temporal and spatial resolution. The increase in imaging speed is based on the assumption that dynamic changes are restricted to a small circular FOV. These changes can be rapidly recorded by angularly undersampled polar imaging without sacrificing spatial resolution. As shown in the THEORY section, the radius of the reduced FOV is directly proportional to the number of equally spaced k -space diagonals. The time resolution of dynamic polar imaging, therefore, depends on the spatial extension of the dynamic changes and can be increased by a factor of 16 for the catheter experiment.

Reduced circular FOV imaging requires no additional *a priori* information on the location of image changes and no additional correction procedures. However, a rough estimation of the extension of possible changes can be used to adapt the undersampling factor. The proposed technique is very robust with regard to changes outside the circular FOV. These changes appear as small streaking artifacts in the reduced FOV, as shown in Fig. 7. This is an important advantage compared with Cartesian undersampling, which is very sensitive to wrapping or aliasing artifacts (7).

Although the new technique was implemented with a reduced circular FOV, different geometric shapes of local FOV are possible by varying the sampling density in angular direction. Oval or elliptic reduced FOV, as shown in Fig. 3, can be generated and adapted to anatomical shapes. Additionally, the presented technique is not limited to two dimensions but can be easily extended to three-dimensional reduced volume measurements. Likewise, sequence types other than the proposed true

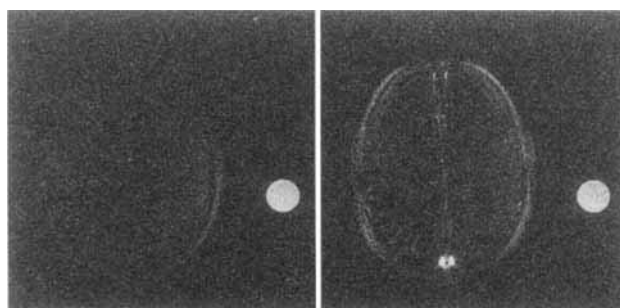


FIG. 7. (a) and (b) are subtraction images calculated from the reference image (head only) and head with water tube. In (b), the head was additionally rotated by a few degrees relative to the reference. The difference image in (a) shows almost no artifacts. (b) shows minimal streaking artifacts since the difference image exceeds the reduced FOV of 38 mm. All gray values are printed with increased brightness and contrast.

FISP can be used. Applications of the reduced FOV technique could include dynamic functional imaging (i.e., the visual cortex), dilations and interventional procedures, and dynamic imaging of pulsatile flow in small vessels.

The primary limitation of this technique is the reduced SNR of the dynamic difference image. Subtraction (or summation) of statistically independent noise decreases the SNR by a factor of $1/\sqrt{2}$. Undersampling also reduces the SNR since the total acquisition is reduced. n -fold undersampling, therefore, reduces the SNR by a factor of $1/n$, since pixel volume or resolution is unchanged. Considering the subtraction procedure, the SNR of the dynamic reduced FOV is decreased by a factor of $1/\sqrt{2}n$ compared with the reference image.

We would finally like to emphasize the favorable intrinsic properties of projection reconstruction-based imaging techniques. This sampling scheme offers advantages in motion and flow artifact suppression, efficient use of gradients, and fast acquisitions. In addition, the coverage of k -space center in each radial diagonal avoids contrast discontinuities and preserves the smoothness of the imaging process (17). Major drawbacks are blurring artifacts caused by a degradation of the PSF by off-resonance effects and a suboptimal sampling efficiency compared with Cartesian sampling.

REFERENCES

1. P. Mansfield, Multiplanar image formation using NMR spin echos. *J. Phys. C: Solid State Phys.* **10**, L55–L58 (1977).
2. W. Irnich, Electrostimulation by time-varying magnetic fields. *MAGMA* **2**, 43–49 (1994).
3. P. Margosian, Faster MR imaging—imaging with half the data, in "Proc., SMRM, 4th Annual Meeting, London, 1985," p. 1024.
4. J. J. van Vaals, M. E. Brummer, W. T. Dixon, H. H. Tuithof, H. Engels, R. C. Nelson, B. M. Gerety, J. L. Chezmar, J. A. den Boer, "Keyhole" method for accelerating imaging of contrast agent uptake. *J. Magn. Reson. Imaging* **3**, 671–675 (1993).
5. R. A. Jones, O. Haraldseth, T. B. Muller, P. A. Rinck, A. N. Oksendak, k -space substitution: a novel dynamic imaging technique. *Magn. Reson. Med.* **29**, 830–834 (1993).
6. L. Yao, Y. Cao, D. N. Levin, 2D locally focused MRI: applications to dynamic and spectroscopic imaging. *Magn. Reson. Med.* **36**, 834–846 (1996).
7. X. Hu, T. Parrish, Reduction of field of view for dynamic imaging. *Magn. Reson. Med.* **31**, 691–694 (1994).
8. F. J. Harris, On the use of windows for harmonic analysis with the discrete Fourier transform. *Proc. IEEE* **66**(1), 51–83 (1978).
9. M. L. Lauzon, B. K. Rutt, Effects of polar sampling in k -space. *Magn. Reson. Med.* **36**, 940–949 (1996).
10. R. N. Bracewell, A. R. Thompson, The main beam and ring lobes of an east-west rotation synthesis array. *Astrophys. J.* **182**, 77–94 (1973).
11. F. Natterer, "The Mathematics of Computerized Tomography," Teubner, Stuttgart, 1986.
12. K. Scheffler, Zooming by back projection, in "Proc., ISMRM, 5th Annual Meeting, Vancouver, 1997," p. 288.
13. V. Rasche, R. W. de Boer, D. Holz, R. Proksa, Continuous radial data acquisition for dynamic MRI. *Magn. Reson. Med.* **34**, 754–761 (1995).
14. L. Axel, G. T. Herman, D. A. Roberts, L. Dougherty, Linogram reconstruction for magnetic resonance imaging (MRI). *IEEE Trans. Med. Imaging* **9**, 447–449 (1990).
15. A. Oppelt, R. Graumann, H. Barfuss, H. Fischer, W. Hartl, W. Schajor, FISP: eine neue schnelle Pulssequenz für die Kernspintomographie. *Elektromedica* **54**, 15–18 (1986).
16. Y. Zur, M. L. Wood, L. J. Neuringer, Spoiling of transverse magnetization in steady-state sequences. *Magn. Reson. Med.* **21**, 251–263 (1991).
17. V. Rasche, D. Holz, W. Schepper, Helical scan for time-resolved MRI at 0.5 T, in "Proc., SMRM, 12th Annual Meeting, New York, 1993," p. 479.